Nanoscale

PAPER

View Article Online
View Journal

Cite this: DOI: 10.1039/d5nr04400f

Fe-doped carbon dots as dual-mode T_1/T_2 nano-contrast agents for ultra-high field MRI

Beatriz Sierra-Serrano, [a,b] Elisa Sturabotti, *[a] Lucia Cardo *[a] and Maurizio Prato *[a,c,d]

Carbon dots (CDs) doped with iron are valuable nano-contrast agents (nCAs) for magnetic resonance imaging (MRI) owing to their optimal compatibility, stability and interesting relaxivity, even at ultra-high fields (UHF-MRI, ≥7 T). Moreover, they represent suitable alternatives to Gd-based contrast agents frequently associated with moderate toxicity. Notably, UHF-MRI offers enhanced spatial resolution and improved signal-to-noise ratios, challenging some limitations encountered for standard MRI of vascular tissues, brain or applications demanding high sensitivity. The design of nCAs for UHF-MRI is not straightforward due to their tendency to show predominant T_2-character at high fields, hence leading to image darkening and resolution loss. For this reason, we propose novel Fe-doped CDs (Fe@CDs) working as dual mode T_1/T_2 nCAs for UHF-MRI; as a grounding concept, our synthesis was supported by stringent purification, a practice extremely overlooked in the CD field. Pure Fe@CDs (Fe content 3.7%) were isolated from fluorescent molecular-like subproducts and uncoordinated metals by size exclusion chromatography (SEC-HPLC); the particles showed good dimensional homogeneity (AFM = 5.0 ± 2.2 nm; TEM = 4.0 ± 1.3 nm), with blue centered and typical wavelength-dependent fluorescence. The structure of Fe@CDs was enriched in carboxylic moieties, enabling stable coordination of iron (in a mixed +2/+3 oxidation state), and optimal *in vitro* safety was observed on A549 cell line at the highest concentration investigated (500 mg mL^{-1}). Fe@CDs presented low r_2/r_1 ratios at high fields, behaving as T_1/T_2 dual-mode probes (r_2/r_1@7 T = 2.78 and r_2/r_1@11.7 T = 3.23); notably, the magnetic properties remained almost unaltered for 8 days in water and cellular medium. Our results provide a combined and wide approach for synthesizing artifact-free Fe-doped CDs with potential in advanced UHF-MRI techniques.

Received 19th October 2025,
Accepted 23rd February 2026

DOI: 10.1039/d5nr04400f

rsc.li/nanoscale

Introduction

Carbon dots (CDs) are classified as carbon-based nanomaterials that possess quasi-spherical morphology, sizes below 10 nm and intrinsic luminescence. Among the various applications, CDs have been widely employed in biomedicine due to their excellent water solubility, photochemical properties, excellent cyto- and biocompatibility and peculiar surface chemistry, with readily functionalizable moieties that allow grafting of drugs, peptides, antibodies, *etc.*[1–3] The luminescence features can be tuned by selecting suitable precursors, choosing optimal doping strategies and varying synthetic parameters (*e.g.*, reaction times, temperatures, *etc.*) in top-down or bottom-up approaches.[4,5] Designing effective combinations of synthetic conditions and setting up the right purification strategies are current challenges in the field for modulating the chemical and physical properties of CDs and to achieve the desired functions for the intended application, still with reliable structures/features. For example, loading CDs with metal ions (*e.g.*, transition metals or lanthanides) is one of the approaches employed to control their electrocatalytic or magnetic properties, hence endowing the material with additional functions useful in therapy, bio-catalysis and bioimaging.[6–9] In particular, CDs doped with paramagnetic metal ions, such as gadolinium (Gd^{3+}), manganese (Mn^{2+}), or iron (Fe^{3+}/Fe^{2+}), are emerging as interesting multifunctional nanoparticles (NPs) capable of generating contrast in magnetic resonance imaging (MRI). Doping with Fe further enabled antibacterial activity against *Escherichia coli* or *Hafnia alvei*, inducing oxidative stress, altering cellular metabolism or mimicking peroxidase-like behavior,[10] induced apoptosis and immunity response and prevented metastasis in mice bearing

[a]*Center for Cooperative Research in Biomaterials (CIC biomaGUNE), Basque Research and Technology Alliance (BRTA), Paseo de Miramon 194, 20014 Donostia-San Sebastián, Spain.*
E-mail: esturabotti@cicbiomagune.es, lcardo@cicbiomagune.es, mprato@cicbiomagune.es
[b]*University of the Basque Country (UPV-EHU), 20018 Donostia-San Sebastián, Spain*
[c]*Ikerbasque, Basque Foundation for Science, 48013 Bilbao, Spain*
[d]*Department of Chemical and Pharmaceutical Sciences, INSTM UdR Trieste, University of Trieste, 34127 Trieste, Italy*

tumors.[11] Moreover, Fe^{2+}/Fe^{3+}-based CDs, CD/NPs composites or NPs, in general, have found extensive use in Fenton and Fenton-like reactions, useful as cancer treatment agents.[12,13] In terms of diagnostic applications, MRI is one of the most important non-invasive and non-ionizing imaging techniques in clinics, which allows the acquisition of 3D images of tissues in the body with high spatial resolution.[14] This technique is based on the principles of nuclear magnetic resonance: protons, primarily from water in tissues and organs, are aligned by an external magnetic field and then excited using radio frequency (RF) pulses; upon cessation of the pulses, the protons return to their equilibrium state through two possible relaxation processes: (i) longitudinal relaxation (r_1, recovery along the magnetic field axis), characterized by relaxation time T_1, and (ii) transversal relaxation (r_2, loss of phase coherence in the plane perpendicular to the magnetic field), characterized by relaxation time T_2. MRI images are generated upon detection and processing of T_1 and T_2, which are highly dependent on the local molecular environment of the protons; therefore, they vary across different tissue types and biological conditions, generating contrast in the resulting images. However, natural contrast is sometimes insufficient, so contrast agents (CAs) are administered before MRI scans to enhance imaging and avoid loss of information.[15] CAs work by affecting T_1 or T_2 (depending on the agent employed) in specific areas of interest (cells, tissues, veins, *etc.*): T_1 CAs accelerate longitudinal relaxation, producing brighter images (positive contrast), while T_2 CAs shorten transverse relaxation, resulting in darker images (negative contrast). The efficiency and typology of CAs are defined by relaxivity values (r_1 and r_2), representing how relaxation rates change with the compound concentration. The CAs employed in clinics for decades are coordination complexes of Gd^{3+}, such as Magnevist® (Gd-diethylenetriaminepentaacetic acid, Gd-DTPA), Omniscan® (Gadodiamide) and others (T_1-CAs).[16,17] However, significant safety concerns are associated with Gd-based CAs,[18,19] mainly related to possible release of Gd^{3+} ions with consequent accumulation in tissues and organs, a major concern particularly for patients requiring repeated CA injections. Therefore, there is a growing demand for novel CAs for MRI, which are able to mitigate the safety risks linked to Gd-based CAs without compromising optimal contrast efficiency and biodistribution. At the same time, the continuous advances in bio-nanotechnology enable the design of multimodal nanoscale contrast agents (nCAs) as MRI-active probes, which are also able to deliver additional functions such as therapeutic activity, bio-targeting or complementary diagnostic modes.[16,20] Superparamagnetic iron oxide nanoparticles (SPIONs) are a notable example in this direction, since they are the first nCAs able to achieve clinical use as an alternative to Gd-based CAs (*e.g.*, ferumoxytol (Feraheme®/Rienso®) and others).[21] SPIONs have been combined to CDs for obtaining nanohybrids to scavenge free radicals, trigger osteochondral tissue regeneration and, most importantly, to work as dual-mode imaging agents, providing simultaneously fluorescence signals and MRI contrast.[22,23] However, a few SPION formulations have been discontinued or withdrawn from the market due to regulatory issues, unsatisfactory clinical benefits or manufacturing costs.[24] Paramagnetic metal-based nCAs are highly promising, especially if based on Mn or Fe, since these are essential elements in the body and lower toxicity profiles are expected. Furthermore, in high-spin Fe-based CAs, the metal is a strong Lewis acid hence the binding of the metal within the chelating environment is highly stable, minimizing the risk of dissociation.[25,26]

Another important aspect concerns the recent advancement of ultra-high field (UHF) MRI systems, which operate at magnetic field strengths beyond 7 T. These systems offer significantly enhanced spatial resolution and improved signal-to-noise ratios compared to previous low-field MRI technologies, making them particularly valuable for non-invasive imaging of brain or tumor vasculature with high sensitivity.[27–30] Key limitations in UHF-MRI include: (i) the prolonged T_1 relaxation times of tissues, which reduces the effectiveness of traditional T_1 contrast agents and (ii) the r_1 of several CAs and nCAs decreases at high external magnetic fields, also compromising the effectiveness of the contrast at safe doses.[31] In other words, most imaging probes reported in the literature so far are paramagnetic or superparamagnetic species that induce strong T_2-decay at UHF, impeding T_1 contrast enhancement. Consequently, the development of T_1 imaging probes that are tailored to the UHF platform is challenging but it is crucial to fully realize the sensitivity of UHF-MRI.[32]

In this context, biocompatible Fe-based nanomaterials are intensively explored as versatile systems in which the Fe^{2+}/Fe^{3+} ratio, particle sizes and morphologies can be controlled and tailored to achieve specific relaxivity properties even at UHF. Compared to more conventional metal oxide nanoparticles, CDs can be prepared through fast, easy, economical and, ideally, scalable "one pot" reactions without the need for additional coating procedures for their stabilization. The vast realm of synthetic options, although with some uncertainties,[9,33] makes CD design and functionalization broadly versatile; these nanoparticles may be finely shaped on demand for overcoming toxicity issues, low targeting, fast excretion rates and fluorescence tagging, usually associated with other types of nanomaterials (*i.e.*, quantum dots or SPIONs).[34] Metal-doped CDs are usually photochemically stable systems, water soluble and safe-by-design, while offering high versatility for the incorporation of additional therapeutic functions; their intrinsic luminescence enables multiple diagnostic modalities, working as combined fluorescent/MRI probes. Furthermore, depending on the synthetic design, the structural framework of water-soluble CDs can be modulated to enhance water permeability.[35] The accessibility of water to the metal coordination environment within the nanoparticle is preferred, as this could positively affect relaxation times and improve the magnetic response of the material in aqueous and biologically relevant media.[36]

The scope of this work was to explore the possibility of incorporating Fe within carbonaceous CDs and generate a system with adequate relaxivity for UHF-MRI. For this specific application, very few analogous systems have been proposed in

recent years, showing, as proof-of-concept, that Fe-CD systems are suitable to generate contrast in MR images in *in vivo* experiments at low fields.[37–41] In almost all cases, carbon particles are doped with Fe^{2+}, which is the least desirable oxidation state due to increased toxicity risks.[42] Wang and coworkers developed an interesting Fe^{3+}-CD hybrid,[40] although here, the carbon NPs act as "ligands" in post-synthetic metal coordination, rather than being employed as the host matrix of the metal. Herein, we intend to focus on Fe^{3+}, selected as one of the precursors in bottom-up synthesis, since ultrasmall NPs based on Fe^{3+} are safer and particularly suitable for UHF-MRI.[43] Notably, our fluorescent nanoparticles exhibited promising relaxivity values that increase under higher magnetic fields, behaving as a valuable T_1/T_2 dual mode probe. At the same time, the system developed here was employed as a case study to demonstrate the importance of combining synthesis and purification/characterization methodologies in order to obtain reliable Fe-doped CDs with improved performances as magnetic NPs. Purification is currently a hot topic in the field of metal-doped CDs, or CDs in general, and strong efforts are still required to finally obtain artifact-free nanomaterials.[9] We also discuss the challenges associated with avoiding mixed Fe oxidation states under the extreme reaction conditions required for the synthesis of CDs. Currently, this is a critical point toward the achievement of well-defined Fe-CD formulations and very poorly discussed in previous reports. We believe that our combined experimental setup, although defined on a specific class of Fe-doped CDs, has wide scopes and applicability, offering a firm methodology for obtaining pure metal-doped CDs.

Results

The bottom-up synthesis of CDs was performed through a microwave-assisted method using β-alanine (β-Ala), ethylenediaminetetraacetic acid (EDTA) and iron(III) chloride hexahydrate ($FeCl_3{\cdot}6H_2O$) as precursors. Building on our own and others' expertise,[8,44] β-Ala and EDTA were selected as the carbon/nitrogen source. The presence of both $-NH_2$ and –COOH groups in β-Ala and EDTA makes the two starting materials "chemically compatible", an aspect that is crucial for initiating the polymerization, condensation and carbonization processes under microwave-assisted hydrothermal conditions (240 °C, 300 W) and generating the fluorescent CDs. Amino acids are ideal building blocks owing to their benign nature, abundance of reactive functional groups and a small common scaffold with an interchangeable side chain; together with β-Ala, EDTA is essential to generate the main CD carbonaceous structure, reasonably *via* the formation of a polyamide-based crosslinked network. The residual carboxylic functionalities enable stable metal ion coordination and encapsulation within the carbon matrix, contributing to the effective Fe doping of the CDs (Fig. 1).[45] The mixture obtained after the hydrothermal reaction was centrifuged, filtered, and dialyzed to afford, upon lyophilization, a brown powder identified as a potential crude Fe-doped CD formulation. The reaction parameters were optimized by screening different combinations of precursor ratios, Fe salts or reaction times (Table 1). Our results indicated that the Fe content (measured by inductively coupled plasma mass spectrometry, ICP-MS) decreased from 10.4% to 6.1% and 5.2% after 30, 45 and 60 minutes, respectively (entries 1, 2 and 4), indicating that extending the reaction time did not improve the Fe doping level. To increase the metal content, the molar amount of $FeCl_3{\cdot}6H_2O$ was doubled, maintaining a reaction time of 45 min (entry 3). However, no increase in Fe doping was observed in the crude product. The decrease in Fe content with increasing time and/or metallic source amount could be explained considering the harsh synthetic conditions used (high temperature/pressure); indeed, higher amounts of insoluble and iron-rich species may be formed both at longer times and high Fe starting amount and, eventually, removed by filtration. This trend is also reflected by the drastically low yields observed in entries 3 and 4, for which only small amounts of water-soluble and Fe-doped crude materials were collected after dialysis.

A different Fe source was also tested using tris(acetylacetonate) iron(III) ($Fe(acac)_3$, Scheme S1) as a precursor. This compound was selected because it had been previously reported as a reactant for the preparation of water-soluble magnetite particles in organic or hydrophilic solvents.[46,47] However, the yield of the resulting crude Fe-doped CDs was very low (entries 5 and 6). In entry 7, only β-Ala and $Fe(acac)_3$ were employed, while EDTA was excluded from the reaction

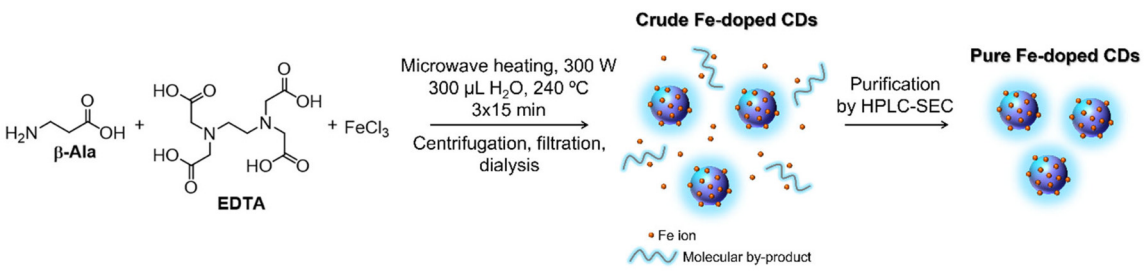

Fig. 1 Graphical representation of the reaction among β-Ala, EDTA and $FeCl_3{\cdot}6H_2O$ to synthesize iron-doped CDs. Nanoparticles are produced in water at high temperature/pressure by microwave-assisted synthesis. After collecting the crude Fe-doped material, pure CDs were isolated from by products using size exclusion chromatography (SEC) combined with high-performance liquid chromatography (HPLC).

Table 1 Reaction parameters investigated to synthesize Fe-doped CDs

Entry[a]	Crude sample	Prec. 1	Prec. 2	Iron source	mmol	t (min)	Yield (%)	Fe% (w/w)	r_1 (mM^{-1} s^{-1})
1	Fe@CDs_1	β-Ala	EDTA	$FeCl_3$	0.25	30	17	10.37	0.81
2	**Fe@CDs**				0.25	45	27	6.10	0.92
3	Fe@CDs_3				0.50	45	3	2.70	—
4	Fe@CDs_4				0.25	60	12	5.20	1.0
5	Fe@CDs_acac1		EDTA	$Fe(acac)_3$	0.25	30	9	4.20	—
6	Fe@CDs_acac2				0.25	45	5	5.46	—
7	Fe@CDs_acac3		—		1	45	—	—	—

All the reactions were performed at 240 °C, with 300 W and in 300 μL of Milli-Q water by means of microwave-assisted synthesis. β-Ala and EDTA are always reacted in 1 mmol each. [a] All the parameters refer to the nanomaterial after the dialysis, *i.e.*, crude carbon dots.

mixture, but no product was obtained under these conditions. This behavior was most likely due to the high stability of the Fe(III)-triacetate complex and its low solubility in aqueous environments, even at elevated temperatures, which appear to hinder carbonization, doping and the colloidal stabilization provided by the CD structure.

Given the potential application of the materials as MRI nCAs, the evaluation of their longitudinal relaxivity (r_1) was a key factor. Among the higher-yielded crude products (entries 1, 2 and 4), entry 2 displayed the highest r_1 value at 1.5 T (r_1 = 0.92 mM^{-1} s^{-1}). Overall, the reaction conditions of entry 2 exhibited the best combination of yield, reaction time and relaxivity properties; therefore, the deriving material was selected as crude_Fe@CDs for further purification studies and characterization.

Dialysis is the most common purification method used for CDs, but we and others have recently shown that it is often insufficient to obtain reliable and artifact-free CDs; hence further purification steps are necessary.[8,48–50] This is particularly recommended for metal-doped CDs, since metal-based molecular species can be formed during the synthesis and remain after dialysis procedures. Indeed, several factors may reduce the efficiency of dialysis, such as slow diffusion, the presence of impurities or aggregates exceeding the membrane cut-off, or formation of adducts among the side products and NPs by electrostatic interactions. The thorough purification of CDs is essential to obtain reliable materials, whose distinct properties are not influenced by ion-doped molecular impurities or small molecular fluorophores. To further investigate this aspect, crude_Fe@CDs were analyzed by gel electrophoresis (GE, lane i in Fig. 2A). This technique is routinely employed by biochemists to separate biomolecules based on their charge, shape and molecular weight and, in some cases, can be adapted to nanomaterials science to evaluate the presence of different NP populations and their respective charges.[51] From GE analysis, crude_Fe@CDs are clearly a heterogeneous mixture composed of positive and negative fluorescent populations. The Fe content in crude_Fe@CDs is found to be ~6% (w/w) through ICP-MS measurements. ICP-MS analysis of the individual populations, separated by cutting the GE plate, confirmed that only the negatively charged fractions contained the metal, whereas the positively charged material was most likely a fluorescent artifact removable from the mixture. This latter aspect highlights the importance of GE as a tool for a first evaluation of the composition of CDs (charge, metal doping, heterogeneity) after dialysis. Size exclusion chromatography (SEC) combined with high-per-

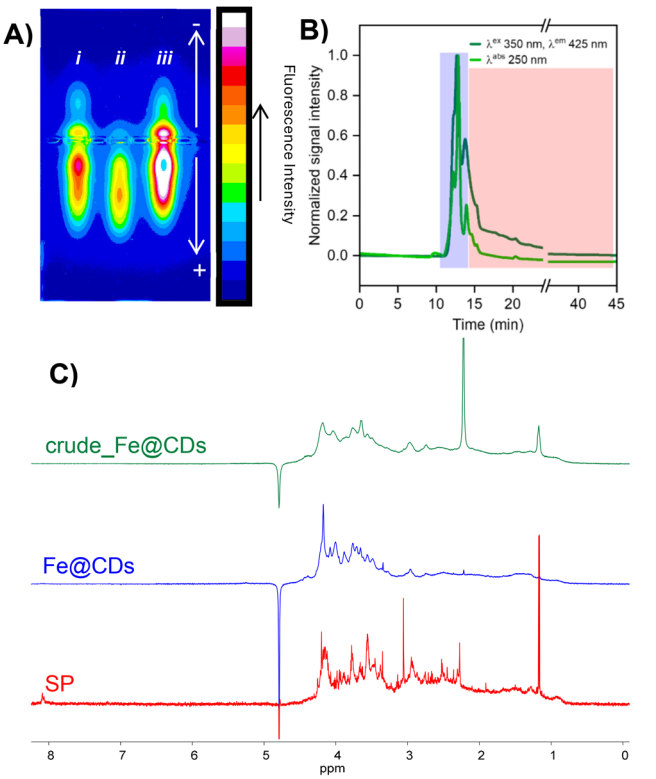

Fig. 2 (A) Gel electrophoresis (1% agarose in 1× TAE buffer) of (from left to right): (i) crude_Fe@CDs showing both negatively and positively charged populations of the material, (ii) pure CDs, *i.e.*, Fe@CDs (eluted from 11–14 min in SEC-HPLC), showing the separated negatively charged population, and (iii) side products (SPs) (eluted from 14–45 min in SEC-HPLC) as mixed charge side products. Samples, dissolved at 10 mg mL^{-1} concentration in water, were loaded in the middle of the gel. (B) Chromatograms (obtained by SEC-HPLC) of crude_Fe@CDs by recording absorbance (at 250 nm) and fluorescence ($\lambda^{ex}/\lambda^{em}$ = 350/425 nm). The fractions collected as purified CDs and side products (SPs) are highlighted (blue and red boxes, respectively). (C) ^{1}H-NMR spectra (D_2O) of crude CDs (green), purified CDs (blue) and SPs (red). After purification, the spectrum of Fe@CDs appears broad with signals spanning between 2 and 4.5 ppm in D_2O.

formance liquid chromatography (HPLC) was selected as the purification method on a semi-preparative scale (NH_4HCO_3, 50 mM, pH = 8.3 as eluent). This method allows separation of NPs from molecular species by means of their hydrodynamic radius (or their effective size in the eluent employed). In SEC, the stationary phase pores act as molecular sieves and, considering the column employed (working within a molecular weight range of 100–5000 Da, see the Materials and Methods section), CDs are expected to be eluted at lower retention times (rt) compared to the lower molecular weight side products. The alkaline pH of the aqueous eluent allowed us to separate the nanomaterials without losing the metallic ions coordinated in the CD nanostructure. All chromatograms were recorded by monitoring both absorbance (250 nm) and emission ($\lambda^{ex}/\lambda^{em}$ = 350/425 nm) of the eluted samples. The profile of crude_Fe@CDs (in Fig. 2B) confirmed the heterogeneity of the mixture after dialysis, containing fluorescent components of different charges (as suggested by GE analysis) and sizes. Based on an analogous study recently reported by our group,[44] we collected the fraction between 11 and 14 min rt (the blue box highlighted in the chromatogram), displaying higher fluorescence. Separately, we collected all the fluorescent material eluted as a long tail from 14 to 45 min (red box). The fractions are referred to as Fe@CDs and the side products (SPs), respectively. GE analysis of the isolated Fe@CDs (Fig. 2A, lane ii) displayed a narrower distribution of only the negatively charged material, whilst the SP showed a heterogeneous composition comparable to that of the crude sample (Fig. 2A, lane iii). Therefore, the SEC-HPLC procedure enabled the separation of the Fe-doped negatively charged material from a mixture of undesired emissive side products, likely characterized by a lower molecular weight or hydrodynamic radius under the elution conditions that were employed in SEC. The separation by SEC afforded a 70% recovery of Fe@CDs compared to the crude sample injected and contained 3.7% (w/w) of metal. The loss of metal compared to the initial crude sample was not surprising; our group observed a similar behavior in other metal-doped CDs after purification, confirming that low molecular weight Fe-complexes or weakly coordinating Fe ions are part of the crude composition.[8] The nanomaterials were analyzed by ^{1}H-NMR as a further complementary tool to evaluate the presence of impurities in the CDs. The spectrum of crude_Fe@CDs (Fig. 2C, green spectrum) displayed a set of broad signals ranging from 0.5 to 4 ppm, suggesting the formation of an aliphatic CDs network, in line with the precursors used, while signals ascribed to the starting materials were absent (Fig. S1, black spectra); other sharp peaks, usually ascribed to molecular side products, were not detectable.[52] However, the ^{1}H-NMR spectrum of Fe@CDs after separation by SEC-HPLC also exhibited a very broad profile (blue spectrum), whereas the spectrum of the SP fraction showed several sharp signals typical of molecular species. Therefore, their removal from the final Fe@CDs formulation was eventually relevant. This suggests that NMR analysis of CDs is a valuable tool for a preliminary evaluation of the formation of material-like species, especially when screening different synthetic conditions.[48] However, the sole NMR analysis does not allow conventional signal assignment or necessarily exclude the presence of impurities, particularly when they overlap with the signals of the CDs. In this case, our results demonstrated that chromatographic purification was essential to remove molecular species that were masked in the NMR profile of the crude material.

Overall, we propose that a proper validation of the quality/performance of CD formulations should rely on the combined application of multiple analytical techniques and, when required, different purification protocols should be evaluated.

The UV-vis spectra of crude and purified CDs are presented in Fig. 3A. Both CDs displayed typical absorption profiles in the UV region. The two main peaks, centered at 270 nm and 330 nm, are referred to the $\pi \rightarrow \pi^*$ transition of sp^2 carbons and the intrinsic absorption of the $n \rightarrow \pi^*$ transition of C═O.[53] The UV-Vis profiles of the two nanomaterials did not show major differences; however, the purification impacted the fluorescence of our dots (Fig. 3B). Both crude_Fe@CDs and Fe@CDs showed the wavelength-dependent emission, commonly reported for CDs;[54,55] nevertheless, the emission maximum (λ^{em}_{max}) of Fe@CDs was shifted from 420 nm (λ^{ex} = 350 nm) to 400 nm (λ^{ex} = 325 nm) and other emission bands upon excitation at higher wavelengths (*i.e.*, λ^{ex} = 375 and 400 nm) displayed relatively lower intensities (~50% decrease) after purification. Changes in the fluorescence profiles, together with the reduction of the Fe content in the Fe@CDs, are ascribable to the removal of blue emitting and metal-doped (molecular) byproducts by SEC-HPLC chromatography, overshadowing CD true features (byproducts appear as fluorescent materials in the gel in trace iii of Fig. 2A). The formation of fluorescent impurities during the bottom-up chemical synthesis of CDs is a recurring phenomenon that can occasionally lead to molecular fluorophores becoming the exclusive contributors to CD emission.[56] To avoid misleading and erroneous interpretation, CD isolation should become a common practice in laboratories; our results demonstrate how the combination of several characterization and purification techniques significantly affects both optical properties and metal content, improving CD composition and purity, factors that are essential for CD-related applications.

The morphology of Fe@CDs was analyzed by atomic force microscopy (AFM, probing the *z*-axis) and transmission electron microscopy (TEM, allowing for measuring along the *x*–*y* plane), as shown in Fig. 4A and B, respectively. Comparing both analyses, spherical-like nanoparticles were detected, providing comparable size distributions: 5.0 ± 2.2 nm by AFM and 4.0 ± 1.3 nm by TEM. Local crystallinity was not observed in the TEM images. These results are consistent with previous reports, confirming that the mixture of β-Ala, EDTA and metal ions generates under microwave assisted synthesis at 240 °C metal-doped NPs with an amorphous structure.[8,44]

The chemical composition of the CDs was analyzed by X-ray photoelectron spectroscopy (XPS in Fig. 5). It was determined that the Fe@CDs were mainly composed of carbon (68.3%), nitrogen (9.8%), oxygen (21.2%) and iron (0.7%) (atomic per-

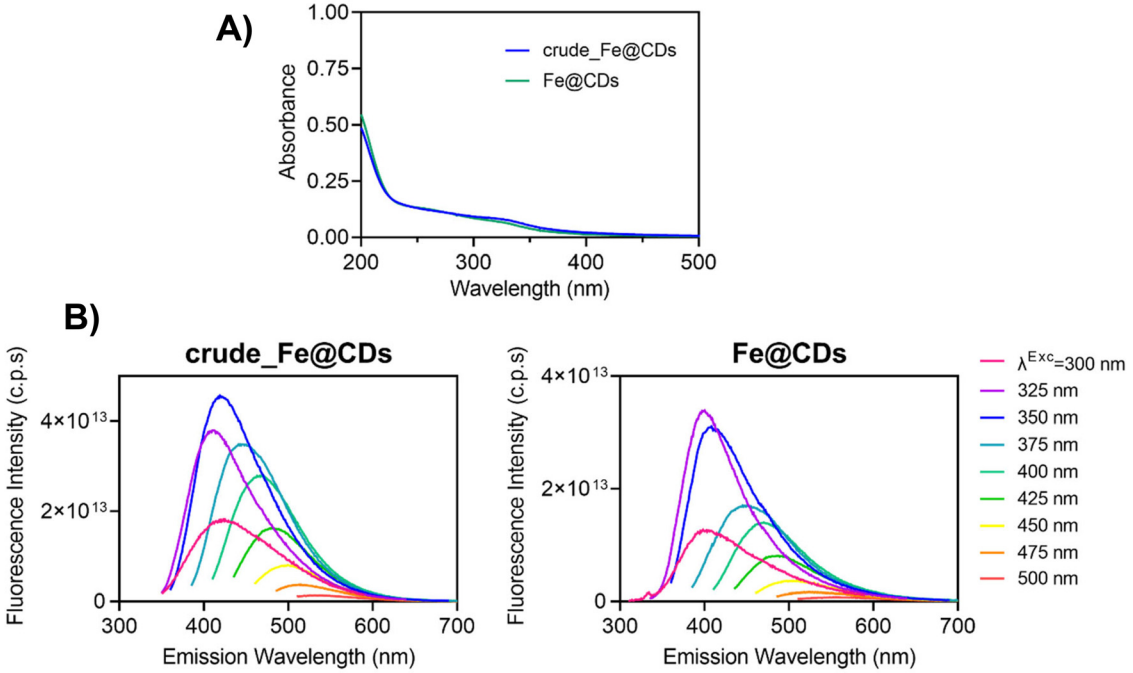

Fig. 3 (A) UV-vis spectra of crude_Fe@CDs and Fe@CDs. (B) Emission spectra of crude_Fe@CDs (left) and Fe@CDs (right).

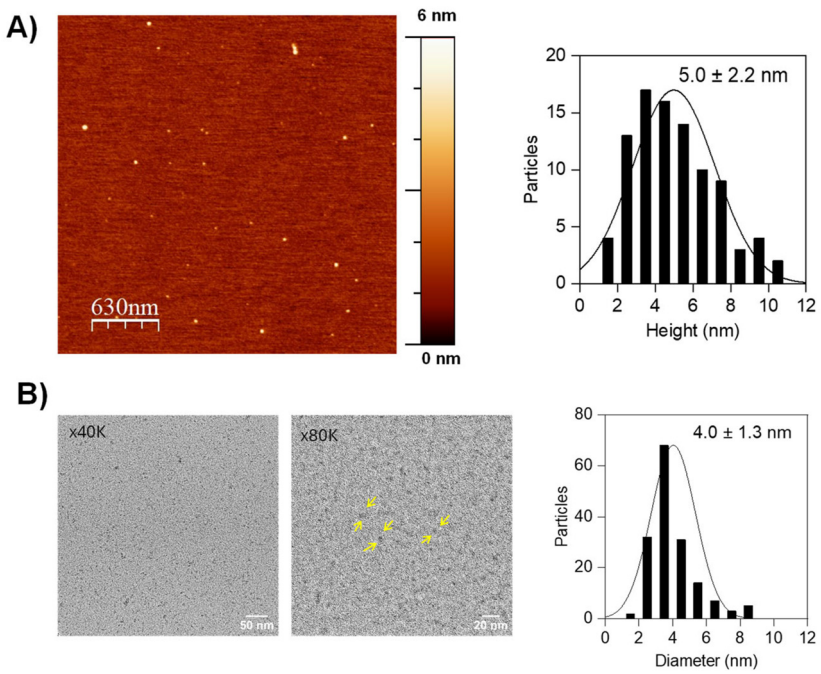

Fig. 4 (A) AFM image (left) and size distribution (right) of Fe@CDs. (B) TEM images (at 40k and 80k magnifications, left and center, respectively) and size distribution (right) of Fe@CDs. The yellow arrows point at carbon NPs (lower contrast at higher magnification).

centage for each element). By converting these data to mass percentage, 3% Fe (w/w) was obtained, which is in good correlation with the ICP-MS result (see above). XPS analysis of carbon, nitrogen and oxygen confirmed that the CDs are composed of a variety of chemical functionalities. Deconvolution of the high-resolution C 1s spectrum reveals four peaks centered at 284.8 eV (C–C/C═C), 286.0 eV (C–O), 287.8 eV (C═O) and 288.8 eV (O–C═O), respectively. The latter signal is consistent with the presence of $-COO^-$ groups in the CD network, as also corroborated from the negative profiles seen in the GE

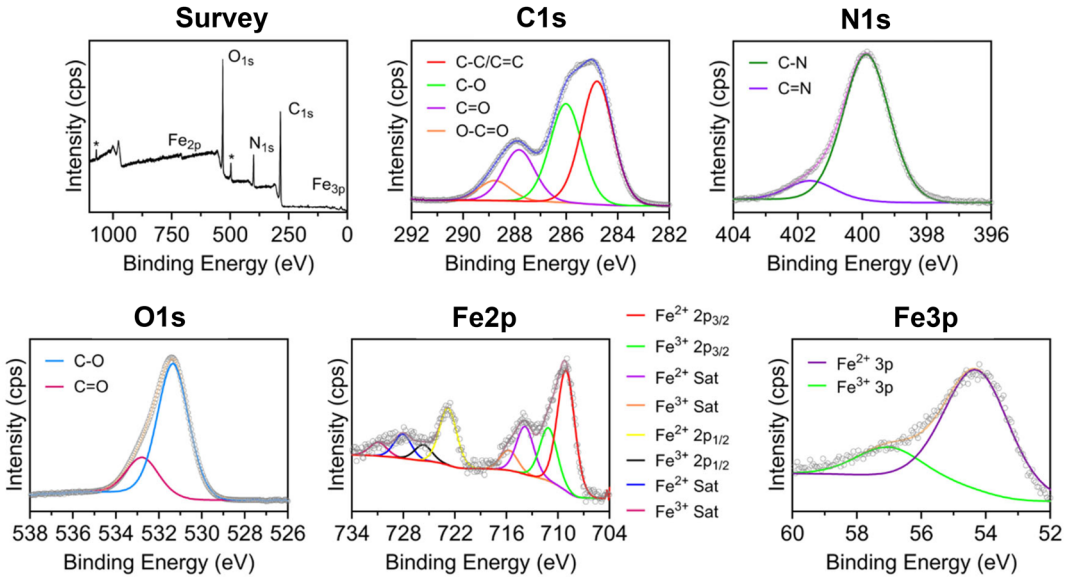

Fig. 5 XPS spectra of Fe@CDs. The grey dots represent the raw data, while the colored lines represent the fitting curves. Carbon, nitrogen and oxygen are the main elements composing the NPs, as evidenced from the survey spectrum (* in the survey spectrum indicates Na^+ impurities). For each element, the high-resolution spectra are also reported (C 1s, N 1s and O 1s). Fe doping (3% w/w) was confirmed by the Fe 2p and Fe 3p peaks (visible in the survey and high-resolution spectra).

analysis. N 1s was deconvoluted into two signals at 399.9 eV and 401.6 eV, ascribable to C–N and C═N contributions. The O 1s spectrum presented signals at 531.3 eV and 532.8 eV for the C–O and C═O moieties, respectively. The presence of iron was highlighted by the signals at around 720 eV and at 55 eV, for Fe 2p and 3p. Splitting of the spin–orbit components of Fe 2p resulted in Fe $2p_{3/2}$ and Fe $2p_{1/2}$ peaks (centered at around 712 eV and 725 eV). By the deconvolution of these peaks, signals for Fe^{2+} and Fe^{3+} were simultaneously evidenced.[57–59] Fe^{2+} was characterized by Fe^{2+} $2p_{3/2}$ band at 709.1 eV and Fe^{2+} $2p_{1/2}$ at 722.8 eV ($\Delta Fe^{2+} \approx 13$ eV) and by two additional satellite peaks (Fe^{2+} $2p_{3/2}$ Sat = 713.8 eV and Fe^{2+} $2p_{1/2}$ Sat = 728.1 eV), commonly encountered in high-spin species.[60] $2p_{3/2}$ and $2p_{1/2}$ signals for Fe^{3+} were also visible in the XPS spectrum at 711.1 eV and 725.7 eV ($\Delta Fe^{3+} \approx 14$ eV) with the corresponding satellites (715.7 eV and 730.9 eV). The presence of mixed valence was also confirmed by the 3p signals[58], as deconvolution of the 3p band revealed two distinct components, Fe^{2+} 3p at 54.3 eV and Fe^{3+} 3p at 57.0 eV. We and others have experienced this behavior, most likely because of the mild oxidizing character of Fe^{3+} (and thus its tendency to be reduced under the synthetic conditions of CDs).[41,61,62] The oxidation state of Fe is hard to control, since partial oxidation/reduction may occur depending on temperature, pressure or solvent contributions.[63] Nevertheless, CD synthesis requires harsh conditions, such as high temperature and pressure,[64] which are critical for the successful formation of the nano-organic frameworks. We confirmed that milder reaction conditions, eventually preferable to avoid Fe oxidation/reduction, negatively interfered with the formation of CDs; reactions performed at lower temperatures (*i.e.*, 200 °C) significantly affected the carbonization process between β-Ala and EDTA and a large fraction of the precursors remained insoluble at the bottom of the microwave vessel (data not shown).

Beyond this synthetic outcome, the presence of mixed-valence Fe^{2+}/Fe^{3+} doping within the CDs does not disqualify the material from being considered as a potential nCA. Overall, the magnetic performances and biosafety of Fe-based NPs, their activity as T_1 or T_2 nCAs, depend on the combination of multiple factors including particle size, surface charge/modification, coating composition, structural features (*e.g.*, crystallinity) and the relative Fe^{2+}/Fe^{3+} composition.[65]

As a basic evaluation of the suitability of Fe@CDs in biological environments, their cytotoxicity was tested in A549 cells (human lung adenocarcinoma) using the MTT assay before and after SEC-HPLC purification. The cells were incubated with increasing concentrations of Fe@CDs for 24 and 48 hours, ranging between 10 and 500 μg mL^{-1}. As shown in Fig. 6, no significant toxicity was evidenced even at high concentrations of the nanoparticles (500 μg mL^{-1}) and after 48 hours of incubation, with ~70% cell survival both for pure and crude quantum dots (Fig. S2). This result confirms that β-Ala and EDTA are a valuable set of precursors to generate metal-doped CD frameworks that guarantee high compatibility in cellular environments. Purification seems to not affect viability, reasonably due to the benign nature of the precursors involved; nevertheless, the removal of side products (see the purification details above), whose formation is ubiquitous during CD synthesis, is central to avoid inconsistencies and flaws in the CDs, as recently pointed out by several authors and our group.[8,9,50,66,67] Additionally, purification by SEC-HPLC had a notable effect on nanomaterial dispersibility:

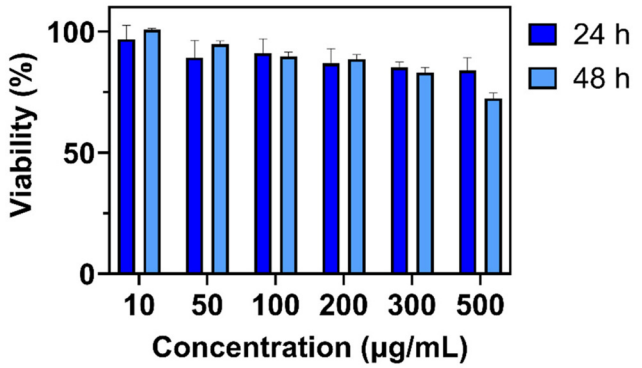

Fig. 6 Viability of the A549 cell line tested using the MTT assay after incubation with Fe@CDs at different incubation times (blue for 24 hours and light blue for 48 hours).

the purified material remained well dispersed in water—even at high concentrations—while the crude one exhibited significantly reduced dispersibility (Fig. S3). This aspect is most likely related to the removal of insoluble Fe-based species and fluorescent molecular like-byproducts (Fe content and fluorescence intensity diminish after SEC-HPLC), further stressing the need for sharp purification of crude products.

Finally, to assess the magnetic properties of the Fe@CDs nanoparticles, their longitudinal and transversal relaxivities were recorded at 1.5 T, 7 T and 11.7 T. The results are displayed in Fig. 7 and collected in Table 2.

The longitudinal and transversal relaxivities of Fe@CDs at 37 °C were 1.38 mM^{-1} s^{-1} and 2.22 mM^{-1} s^{-1} at the lower field. Interestingly, these values are higher than those obtained for crude_Fe@CDs under the same parameters (r_1 = 0.95 mM^{-1} s^{-1} and r_2 = 1.12 mM^{-1} s^{-1}), despite the lower percentage (w/w) of the metal in the pure Fe@CDs. This also highlights the pivotal role of purification in the preparation of nanomaterials with enhanced performances. The longitudinal to transversal relaxivity ratio (r_2/r_1) is generally used to determine whether a material behaves as a T_1 or T_2 contrast agent; ratios lower than 4 suggest T_1 behavior, whereas values above 4 indicate a shift toward dual T_1/T_2 or T_2 behavior.[20] For Fe@CDs, the r_2/r_1 value was 1.61, suggesting T_1 behavior of the nanoparticles at 1.5 T, unlike what is commonly observed with other Fe NPs (dimension above 5 nm), for which the T_2 mechanism is more prominent.[22,68] Our Fe@CDs share a similar T_1 trend with some ultrasmall iron oxide nanoparticles,[69,70] reasonably owing to their small dimensions, which maximize the interaction with water molecules favoring spin–lattice relaxation;[71] in addition, their r_2/r_1 is comparable to that of commercial Gd-based CAs (typically 1.1–1.2; see Table S1), further confirming the predominant T_1 character at low field strengths.[72]

Table 2 Relaxivity values of Fe@CDs at different magnetic fields

Fe@CDs	1.5 T	7.0 T	11.7 T
r_1 (mM^{-1} s^{-1})	1.38	2.16	2.25
r_2 (mM^{-1} s^{-1})	2.22	6.02	7.28
r_2/r_1	1.61	2.78	3.23

Moving to higher fields, the longitudinal relaxivity at 7 T and 11.7 T (21 °C) increased to r_1 = 2.16 mM^{-1} s^{-1} and r_1 = 2.25 mM^{-1} s^{-1}, respectively; the r_2 values reached 6.02 mM^{-1} s^{-1} and 7.28 mM^{-1} s^{-1}, respectively, and relatively low r_2/r_1 ratios were observed (r_2/r_1@7 T = 2.78 and r_2/r_1@11.7 T = 3.23,

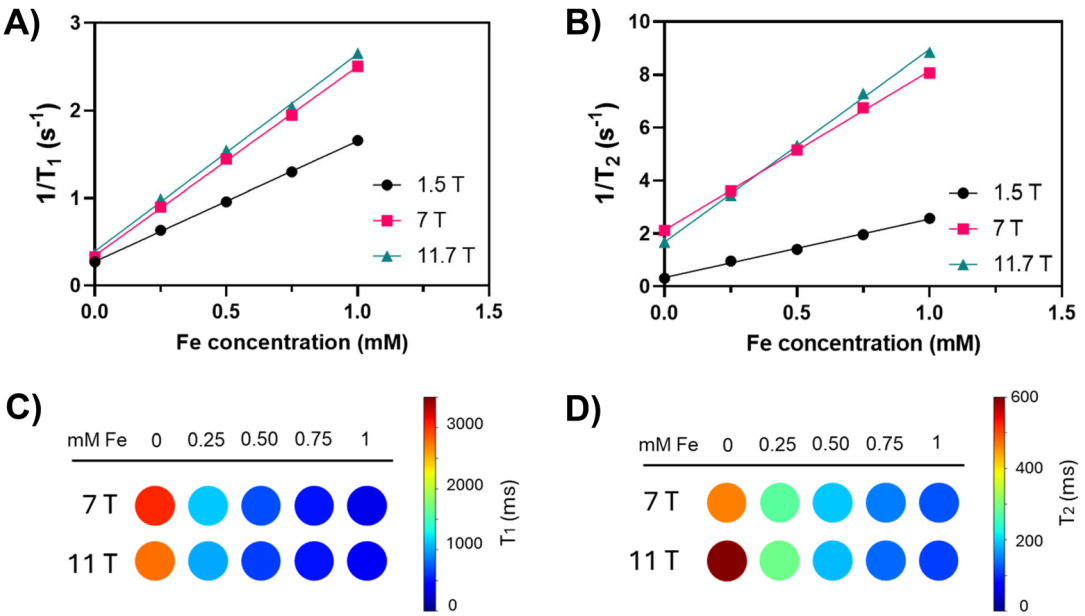

Fig. 7 Magnetic properties of Fe@CDs: (A) $1/T_1$ *vs.* Fe concentration at 1.5 T, 7 T and 11.7 T. (B) $1/T_2$ *vs.* Fe concentration at 1.5 T, 7 T and 11.7 T. (C) T_1 images of Fe@CD phantoms at 7 T and 11.7 T. (D) T_2 images of Fe@CD phantoms at 7 T and 11.7 T.

Table 3 Fe-doped CDs or nanoparticles reported in the literature, selected among the systems tested *in vivo*

Nanoparticle	Field (T)	r_1 (mM^{-1} s^{-1})	r_2 (mM^{-1} s^{-1})	r_2/r_1	Fe oxidation state	Ref.
CDs	1.5	5.8	14.4	2.5	Fe^{3+}-CD complex[a]	40
CDs	3	3.9	4.9	1.3	Fe^{2+}-based CDs	41
CDs	3	1.2	—	—	Fe^{2+}-based CDs	39
CDs	9.4	0.1	9.9	76.1	Fe^{2+}-based CDs	38
Small Fe complex	1	1.4	2.4	1.7	$[Fe(deferasirox)_2]^{3-}$ [b]	25
SPIONs	7	0.9	21.6	25.1	Fe^{3+}-based hematite (α-Fe_2O_3) or maghemite (γ-Fe_2O_3)	30
SPIONs	7	1.4	7.5	5.5	Fe^{3+}-based maghemite (γ-Fe_2O_3)	75
AFNPs	9	2.1	4.1	1.9	$FePt_3$-based antiferromagnetic nanoparticles	32
VSION	9.4	1.1	31.0	27.1	—	76
Ultrasmall Gd_2O_3 nanoparticles	11.7	10.4	17.2	1.6	—	77
Fe-PLGA NPs	14.1	3.0	62.6	20.8	Fe^{3+}-poly-lactic glycolic acid nanoparticles	78

For each example, the following relevant parameters are reported: the magnetic field intensity at which CDs were tested and the relative longitudinal (r_1) and transversal (r_2) relaxivities, the r_2/r_1 ratio and the main oxidation state of Fe. [a] In this system, CDs were employed as a "poly-ligand" in post-synthetic complex formation with Fe^{3+}; therefore, the metal is not part of the carbon matrix. [b] This is an Fe(III) complex.

Table 2). The experimental temperature might play a role in relaxivity enhancement as CAs usually present higher r_1 and r_2 when the temperature is decreased.[31] However, the CA performance is higher at 11.7 T as compared to 7 T, meaning that the enhancement is not (or not only) related to the low temperature difference. This trend differs from what is generally encountered for commercially available Gd-based CAs (in plasma or blood), for which the r_1 values decrease when increasing the magnetic field.[73,74] In Table 3, we indicated several nano-scaled systems selected from the literature, as a comparison with our system. At a lower field, Fe@CDs are comparable to those of many Fe-based nanomaterials that have been effective in *in vivo* MRI scans; however, to the authors' knowledge, only Qin R. *et al.* studied Fe-doped CDs at UHF-MRI *in vivo*, this time working as T_2 nCAs.[38] Our Fe@CDs, showing higher r_1 values at higher magnetic fields and an r_2/r_1 ratio close to 4, could serve as dual T_1/T_2 nCAs for UHF-MRI, alternatively to many agents with an opposite trend (*i.e.*, reduced T_1 performance at higher fields, which compromises sensitivity). It should be highlighted that the *in vivo* performances of nCAs are not determined only by their relaxivities but also by several other factors, including particle size, aggregation and surface coating upon injection in animals, as well as their biodistribution and biokinetics. These will be evaluated in future *in vivo* studies.

Lastly, to assess the long-term stability, we monitored the T_1 of Fe@CDs suspended in water and in cellular medium for 8 days. MRI is highly sensitive to the metal environment; consequently, any kind of aggregation, surface modification or local effects directly affect the relaxation values.[70,79] Fe@CDs remained highly stable at 1.5 T over a period of at least 4 days when dispersed in water. Then, the T_1 signal dropped to around 20% only within the last few days of incubation (Fig. 8A). In the case of cellular growth medium suspensions (RPMI supplemented with 10% fetal bovine serum, 1% L-glutamine and 1% penicillin/streptomycin) at 1.5 T, the T_1 values slightly increased in the first 24 hours, resulting in a lower contrast. This could be explained considering the occurrence of fast associative phenomena among our particles and proteins in the medium that hinders the interaction of the metal center with surrounding water molecules. Similar effects have been noted by others in literature.[79,80] Anyway, after the first 24 hours, the magnetic properties of the mixture remained stable in the full temporal window. At higher fields

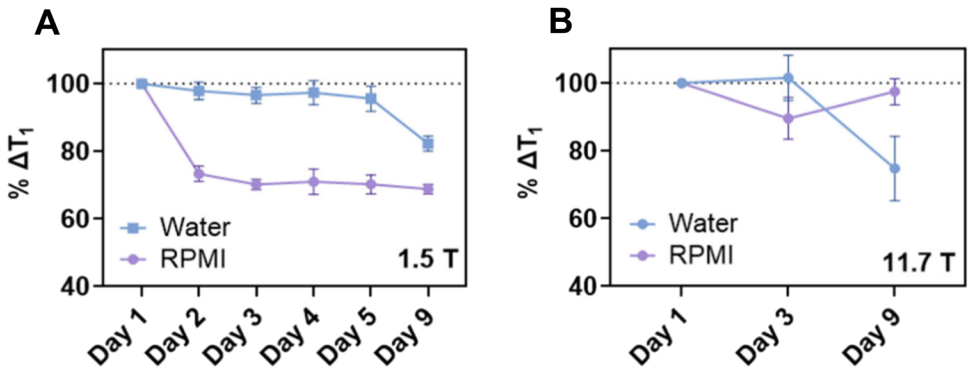

Fig. 8 Eight-day stability of T_1 values for Fe@CDs suspended in water and cellular medium (RPMI supplemented with 10% of fetal bovine serum, 1% L-glutamine and 1% penicillin/streptomycin). Data are presented as a group chart. (A) T_1 monitoring at the lowest field, 1.5 T. (B) T_1 monitoring at 11.7 T.

(Fig. 8B), a 20% reduction in contrast was appreciable at the longest time only for water, while no changes occurred for the dots incubated in RPMI. This evidence is not to be interpreted as a higher stability of the Fe@CDs at 11.7 T; indeed, the fast association of the proteins with the CDs may take place within the first few hours, *i.e.*, in the timeframe occurring among the experiments at the two fields. Eventually, the properties of CDs remain unchanged up to day 8.

Conclusions

In this work, we explored the design, synthesis and purification of Fe-doped CDs, together with their use as nCAs for UHF-MRI. The use of CDs as a hosting matrix of metals is an interesting alternative to the more popular SPIONs, since they allow faster synthetic procedures, tunable properties and intrinsic fluorescence, as additional imaging mode. We discussed the limitations associated with incorporating iron into carbon-based nanoparticles in water, particularly addressing the challenge of controlling its oxidation state (Fe^{3+} *vs.* Fe^{2+}) under the harsh synthetic conditions required for preparing CDs and the solubility of iron-based species. We also proved that the purification of Fe-based CDs by SEC-HPLC is highly important to generate materials free from fluorescent artifacts and other metal-doped/low-molecular weight impurities. This is essential not only as a good synthetic practice but also to ensure accurate data interpretation and, in this context, to maximize the homogeneity and performance of the final Fe@CDs. The nanoparticles showed excitation-dependent fluorescence in the blue-green region and a spherical-like shape of ~5 nm (in diameter and height). The material was highly compatible toward the A549 cell line up to 500 μg mL^{-1} after 48 h of treatment. Regarding the MRI activity, the Fe@CDs behaved as a T_1 contrast agent at 1.5 T, similarly to other few Fe-doped CDs reported in the literature. Moreover, we explored the use of Fe-doped CDs at UHF (7 and 11.7 T). The Fe@CDs showed increased r_1 values with increasing magnetic field and low r_2/r_1 ratios (below 4), indicating a promising dual T_1/T_2 behavior for UHF-MRI. Stability analysis evidenced good properties of the particles in water and cellular medium up to 8 days. These findings may open new opportunities for the use of Fe@CDs as Gd-free CAs and for high resolution MRI purposes. Furthermore, supporting the synthetic procedures with solid purification methodologies represents a convincing workflow to follow for the preparation of robust and well-characterized metal-doped or undoped carbon dots.

Materials and methods

β-Alanine (β-Ala, 99%), ethylenediaminetetraacetic acid (EDTA, anhydrous, 99%) and iron(III) chloride hexahydrate (97%) were purchased from Sigma-Aldrich. Dialysis membrane tubes with molecular weight cut-off of 0.5–1 kDa were purchased from Spectrum Labs. Buffers and solutions for gel electrophoresis and chromatography were freshly prepared using Milli-Q water. Agarose for gel electrophoresis was purchased from Merck.

Synthesis of crude_Fe@CNDs

β-Ala (1 mmol), EDTA (1 mmol) and $FeCl_3 \cdot 6H_2O$ (0.25 mmol) were mixed in 300 μL of Milli-Q water. The mixture was reacted in a Discover 2.0 microwave synthesizer using three consecutive heating cycles. Each cycle corresponded to 15 min of reaction at 240 °C and 300 W. After the reaction, a dark brown mixture was obtained and the precipitate was removed by centrifugation at 4696*g* for 5 min. The recovered solution was filtered with a 0.2 μm filter, followed by dialysis against Milli-Q water for 72 h (MWCO 0.5–1 kDa, water changed three times a day). The solution was freeze-dried and the crude_Fe@CDs (121 mg) were stored in the dark at room temperature.

Gel electrophoresis (GE)

Agarose gel (1% agarose in 1× TAE buffer (40 mM Tris acetate, 1 mM EDTA, pH 8)) was used for GE analysis. Gels of 65 (w) × 100 (l) mm (with a well size of 5 (w) × 1.5 (l) mm) were employed. 7 μL of solutions (10 mg mL^{-1} in Milli-Q water) were loaded into the gel. Electrophoresis was performed using a PowerPac™ Basic Power Supply from Bio-Rad (25 min, 110 V) and the gels were imaged using a Bio-Rad Gel Doc™ EZ imaging system (light source 302 nm and an emission detection system equipped with a chemiluminescence filter 590/110 nm).

Size exclusion chromatography (SEC-HPLC)

High performance liquid chromatography analysis was performed using a Shimadzu SCL-40 equipped with LC-20AR pumps, a CTO-40C column oven, an SPD-M40 photo diode array detector and an RF-20A fluorescence detector. Size exclusion chromatography was performed using an Ultrahydrogel 120 column (120 Å, 6 μm, 7.8 mm × 300 mm, 100–5K, from Waters™) at 0.5 mL min^{-1}, 30 °C and using 50 mM ammonium bicarbonate buffer (pH 8.3) as an eluent.

Optical spectroscopy

UV-Vis spectroscopy was performed using a Varian Cary 5000 spectrophotometer. Fluorescence spectra were recorded using an FS5 Spectrofluorometer (Edinburgh Instruments). In both cases, the measurements were made in Milli-Q water using quartz cuvettes from Hellma® (10 mm path length).

Inductively coupled plasma mass spectrometry (ICP-MS)

CDs were dissolved in nitric acid (1 mL, 67–69%, Optima™, for ultra trace elemental analysis) and then digested using a Speedwave XPERT microwave digestion system. The amount of Fe was measured using iCAP-Q ICP-MS equipped with a collision/reaction cell and Kinetic Energy Discrimination (KED). Sample preparation included dilution with nanopure water (10 mL).

Atomic force microscopy (AFM)

AFM characterization was performed using a JPK bioAFM system using a tapping mode tip with a frequency of 320 Hz (Bruker TESPA-V2). Samples were diluted in Milli-Q water (in the range of ng mL^{-1}) and spin coated on freshly cleaved mica. Images were processed using WSxM 5.0.

X-ray photoelectron spectroscopy (XPS)

XPS experiments were performed using a Versaprobe III Physical Electronics (ULVAC) spectrometer with a monochromatic X-ray source (aluminium Kα line of 1487 eV) calibrated using the 3d5/2 line of Ag at 368.26 eV. The samples were spin-coated on gold-coated 75 × 25 mm slides with 50 nm ± 5 nm Au thickness. XPS data were fitted using CasaXPS software. C 1s, O 1s and N 1s were fitted with the Shirley background and components were adjusted through GL(30) curves.

Cellular studies

A549 cells (human lung epithelial carcinoma) were obtained from the European Collection of Cell Cultures (ECACC), part of the Health Protection Agency. All culture media, reagents, and buffers were sourced from Merck. The cells were maintained at 37 °C in a humidified incubator with 5% CO_2 and 95% air using RPMI 1640 medium supplemented with 10% fetal bovine serum (FBS), 1% L-glutamine, and 1% penicillin/streptomycin. The culture medium was replaced every 2–3 days and the cells were routinely monitored to ensure that they remained contamination-free.

A defined number of cells (4000 per well in 100 μL of medium) were seeded in 96-well plates and allowed to adhere overnight. The following day, the cells were exposed to six different concentrations of pure Fe@CDs, ranging from 10 to 500 μg mL^{-1}, in triplicate. The treated cells were incubated at 37 °C under a humidified atmosphere (5% CO_2, 95% air) for 24 and 48 hours. After incubation, the wells were washed three times with PBS, and 100 μL of MTT solution (0.5 mg mL^{-1} in medium) was added to each well. The plates were then incubated for 3 hours to allow for formazan crystal formation. The medium was carefully removed, and the resulting formazan was solubilized in 150 μL of DMSO. Absorbance was measured at 550 nm using a GENios Pro microplate reader (Tecan). Cell viability data were obtained from three replicates and analysed using GraphPad Prism 9 to generate viability curves.

NMR

A Bruker AVANCE III NMR spectrometer was used to obtain all NMR spectra (11.7 T, 500 MHz for ^1H). Measurements were made in deuterium oxide (99.8% atom D). The spectra were processed using MestReNova.

Relaxivity studies

Relaxation times (T_1 and T_2) were measured in Milli-Q water for different concentrations of CDs using a Bruker Minispec MQ60 (Bruker BioSpin GmbH) contrast agent analyzer at 1.5 T and 37 °C. Experiments at 7 T were performed in water using a Bruker Biospec 70/30 USR MRI system (Bruker Biospin GmbH, Ettlingen, Germany) interfaced to an AVANCE III console. A BGA12 imaging gradient (maximum gradient strength 400 mT m^{-1}) and a 40 mm diameter quadrature volume resonator were used. For T_2 map imaging of the phantoms, the following parameters were adopted: Bruker's MSME (multi slice spin echo) sequence was used. The TE values were varied in 128 steps ranging from 5.5 ms to 704 ms and TR 10 s. For T_1 map imaging of the phantoms, the following parameters were adopted: spin echo saturation recovery using a variable repetition time Bruker's RAREVTR method. Images were acquired at 12 different TR values (7000, 3000, 1800, 1200, 1000, 800, 700, 600, 500, 300, 220, 150, and 55 ms), TE 7.5 ms, and RARE factor 1. All data were acquired with 2 averages, 256 × 256 points and a field of view of 2.56 cm × 2.56 cm, 3 slices with a slice thickness of 2.0 mm and a 2 mm gap between slices. The images were fitted using the Levenberg–Marquardt method to calculate T_1 and T_2 values using Bruker's Paravision 7 software. Experiments at 11.7 T were performed in water using a Bruker Biospec 117/16 USR MRI system (Bruker Biospin GmbH, Ettlingen, Germany) interfaced to an AVANCE III console. An HP 9 imaging gradient (maximum gradient strength 750 mT m^{-1}) and a 40 mm diameter quadrature volume resonator were used. For T_2 map imaging of the phantoms, the following parameters were adopted: Bruker's MSME (multi slice spin echo) sequence was used. The TE values were varied in 128 steps ranging from 5.0 ms to 640 ms and TR 10 s. For T_1 map imaging of the phantoms, the following parameters were adopted: spin echo saturation recovery using a variable repetition time Bruker's RAREVTR method. Images were acquired at 12 different TR values (7000, 3000, 1800, 1200, 1000, 800, 700, 600, 500, 300, 220, 150, 55 ms), TE 7.5 ms, and RARE factor 1. All data were acquired with 2 averages, 256 × 256 points and a field of view of 2.56 cm × 2.56 cm, 3 slices with a slice thickness of 2.0 mm and a 2 mm gap between slices. The images were fitted using the Levenberg–Marquardt method to calculate T_1 and T_2 values using Bruker's Paravision 7 software. In all cases, relaxivity was calculated from the curve fitting of $1/T_1$ or $1/T_2$ (s^{-1}) against the metal concentration (mM) using Graph Pad Prism 9.0.

Conflicts of interest

The authors declare that they have no known competing financial interests or personal relationships that could have appeared to influence the work reported in this paper.

Data availability

The data supporting this article have been included as part of the supplementary information (SI). Supplementary information is available. See DOI: https://doi.org/10.1039/d5nr04400f.

Acknowledgements

All authors wish to thank the funding bodies supporting this research. M. P. is an AXA Professor and is supported by the European Research Council (ERC-AdG-2019, N. 885323) and the Agencia Estatal de Investigación-AEI ("Proyectos I+D+I 2019 – Modalidad Retos Investigación", N. PID2019-108523RB-I00).

References

1 M. Behi, L. Gholami, S. Naficy, S. Palomba and F. Dehghani, Carbon dots: A novel platform for biomedical applications, *Nanoscale Adv.*, 2022, **4**, 353–376, DOI: 10.1039/d1na00559f.

2 L. Đorđević, F. Arcudi, M. Cacioppo and M. Prato, A multifunctional chemical toolbox to engineer carbon dots for biomedical and energy applications, *Nat. Nanotechnol.*, 2022, **17**, 112–130, DOI: 10.1038/s41565-021-01051-7.

3 J. Wang, Y. Fu, Z. Gu, H. Pan, P. Zhou, Q. Gan, Y. Yuan and C. Liu, Multifunctional Carbon Dots for Biomedical Applications: Diagnosis, Therapy, and Theranostic, *Small*, 2024, **20**, 2303773, DOI: 10.1002/smll.202303773.

4 T. Garcia-Millan, T. A. Swift, D. J. Morgan, R. L. Harniman, B. Masheder, S. Hughes, S. A. Davis, T. A. A. Oliver and M. C. Galan, Small variations in reaction conditions tune carbon dot fluorescence, *Nanoscale*, 2022, **14**, 6930–6940, DOI: 10.1039/d2nr01306a.

5 F. Arcudi, L. Đorđević and M. Prato, Design, Synthesis, and Functionalization Strategies of Tailored Carbon Nanodots, *Acc. Chem. Res.*, 2019, **52**, 2070–2079, DOI: 10.1021/acs.accounts.9b00249.

6 L. Lin, Y. Luo, P. Tsai, J. Wang and X. Chen, Metal ions doped carbon quantum dots: Synthesis, physicochemical properties, and their applications, *TrAC, Trends Anal. Chem.*, 2018, **103**, 87–101, DOI: 10.1016/j.trac.2018.03.015.

7 S. A. Rub Pakkath, S. S. Chetty, P. Selvarasu, A. Vadivel Murugan, Y. Kumar, L. Periyasamy, M. Santhakumar, S. R. Sadras and K. Santhakumar, Transition Metal Ion (Mn2+, Fe2+, Co2+, and Ni2+)-Doped Carbon Dots Synthesized via Microwave-Assisted Pyrolysis: A Potential Nanoprobe for Magneto-fluorescent Dual-Modality Bioimaging, *ACS Biomater. Sci. Eng.*, 2018, **4**, 2581–2596, DOI: 10.1021/acsbiomaterials.7b00943.

8 L. Cardo, L. Martínez-Parra, M. Cesco, B. M. Echeverría-Beistegui, M. Martínez-Moro, N. Herrero-Álvarez, M. B. Cabrerizo, S. Carregal-Romero, P. Ramos-Cabrer, J. Ruiz-Cabello and M. Prato, Luminescent Carbon Nanodots Doped with Gadolinium(III): Purification Criteria, Chemical and Biological Characterization of a New Dual Fluorescence/MR Imaging Agent, *Small*, 2023, **19**, 2206442, DOI: 10.1002/smll.202206442.

9 E. Sturabotti, B. Sierra-Serrano, S. M. Apresto, M. Cesco, L. Comparini, L. Cardo and M. Prato, Carbon dots as multi-modal contrast agents: opportunities and open challenges for in vivo bioimaging, *Adv. Drug Delivery Rev.*, 2025, **224**, 115659, DOI: 10.1016/j.addr.2025.115659.

10 C. Huang, M. Duan, Y. Shi, H. Liu, P. Zhang, Y. Zuo, L. Yan, Y. Xu and Y. Niu, Insights into the antibacterial mechanism of iron doped carbon dots, *J. Colloid Interface Sci.*, 2023, **645**, 933–942, DOI: 10.1016/j.jcis.2023.04.149.

11 M. Yang, H. Li, X. Liu, L. Huang, B. Zhang, K. Liu, W. Xie, J. Cui, D. Li, L. Lu, H. Sun and B. Yang, Fe-doped carbon dots: a novel biocompatible nanoplatform for multi-level cancer therapy, *J. Nanobiotechnol.*, 2023, **21**, DOI: 10.1186/s12951-023-02194-6.

12 M. Zhou, Z. Yang, T. Yin, Y. Zhao, C. Wang, G. Zhu, L. Bai, Z. Jiang and W. Zhang, Functionalized Fe-Doped Carbon Dots Exhibiting Dual Glutathione Consumption to Amplify Ferroptosis for Enhanced Cancer Therapy, *ACS Appl. Mater. Interfaces*, 2023, **15**, 53228–53241, DOI: 10.1021/acsami.3c12356.

13 Y. Yang, G. Chen, J. Yu, M. He, M. An, T. Lei, Q. Qin and S. Qin, Fe, N-doped carbon dots/RF in self-Fenton cascade reaction: Improved photodegradation mechanism and toxicity evaluation, *J. Environ. Chem. Eng.*, 2024, **12**, 114151, DOI: 10.1016/j.jece.2024.114151.

14 D. W. McRobbie, E. A. Moore, M. J. Graves and M. R. Prince, *MRI from Picture to Proton*, Cambridge University Press, 2nd edn, 2006.

15 Y.-D. Xiao, R. Paudel, J. Liu, C. Ma, Z.-S. Zhang and S.-K. Zhou, MRI contrast agents: Classification and application (Review), *Int. J. Mol. Med.*, 2016, **38**, 1319–1326, DOI: 10.3892/ijmm.2016.2744.

16 J. Wahsner, E. M. Gale, A. Rodríguez-Rodríguez and P. Caravan, Chemistry of MRI Contrast Agents: Current Challenges and New Frontiers, *Chem. Rev.*, 2019, **119**, 957–1057, DOI: 10.1021/acs.chemrev.8b00363.

17 Z. Gao, T. Ma, E. Zhao, D. Docter, W. Yang, R. H. Stauber and M. Gao, Small is Smarter: Nano MRI Contrast Agents – Advantages and Recent Achievements, *Small*, 2016, **12**, 556–576, DOI: 10.1002/smll.201502309.

18 W. Gwenzi, L. Mangori, C. Danha, N. Chaukura, N. Dunjana and E. Sanganyado, Sources, behaviour, and environmental and human health risks of high-technology rare earth elements as emerging contaminants, *Sci. Total Environ.*, 2018, **636**, 299–313, DOI: 10.1016/j.scitotenv.2018.04.235.

19 K. A. Layne, P. I. Dargan, J. R. H. Archer and D. M. Wood, Gadolinium deposition and the potential for toxicological sequelae – A literature review of issues surrounding gadolinium-based contrast agents, *Br. J. Clin. Pharmacol.*, 2018, **84**, 2522–2534, DOI: 10.1111/bcp.13718.

20 S. Caspani, R. Magalhães, J. P. Araújo and C. T. Sousa, Magnetic nanomaterials as contrast agents for MRI, *Materials*, 2020, **13**, 2586, DOI: 10.3390/ma13112586.

21 T. Vangijzegem, V. Lecomte, I. Ternad, L. Van Leuven, R. N. Muller, D. Stanicki and S. Laurent, Superparamagnetic Iron Oxide Nanoparticles (SPION): From Fundamentals to State-of-the-Art Innovative Applications for Cancer Therapy, *Pharmaceutics*, 2023, **15**, 236, DOI: 10.3390/pharmaceutics15010236.

22 A. Thirumalai, P. Sharmiladevi, K. Girigoswami, A. D. Prabhu and A. Girigoswami, Tuneable carbon dots coated iron oxide nanoparticles as superior T1 contrast agent for multimodal imaging, *ADMET DMPK*, 2025, **13**, DOI: 10.5599/admet.2790.

23 B. Das, A. Girigoswami, A. Dutta, P. Pal, J. Dutta, P. Dadhich, P. K. Srivas and S. Dhara, Carbon Nanodots Doped Super-paramagnetic Iron Oxide Nanoparticles for Multimodal Bioimaging and Osteochondral Tissue Regeneration via External Magnetic Actuation, *ACS Biomater. Sci. Eng.*, 2019, **5**, 3549–3560, DOI: 10.1021/acsbiomaterials.9b00571.

24 R. Vakili-Ghartavol, A. A. Momtazi-Borojeni, Z. Vakili-Ghartavol, H. T. Aiyelabegan, M. R. Jaafari, S. M. Rezayat and S. A. Bidgoli, Toxicity assessment of superparamagnetic iron oxide nanoparticles in different tissues, *Artif. Cells, Nanomed., Biotechnol.*, 2020, **48**, 443–451, DOI: 10.1080/21691401.2019.1709855.

25 L. Palagi, E. D. Gregorio, D. Costanzo, R. Stefania, C. Cavallotti, M. Capozza, S. Aime and E. Gianolio, Fe(deferasirox)2: An Iron(III)-Based Magnetic Resonance Imaging T1 Contrast Agent Endowed with Remarkable Molecular and Functional Characteristics, *J. Am. Chem. Soc.*, 2021, **143**, 14178–14188, DOI: 10.1021/jacs.1c04963.

26 R. Pujales-Paradela, M. Regueiro-Figueroa, D. Esteban-Gómez and C. Platas-Iglesias, Transition Metal-based T1 Contrast Agents, in *Contrast Agents for MRI: Experimental Methods*, ed. V. C. Pierre and M. J. Allen, The Royal Society of Chemistry, 2017. DOI: 10.1039/9781788010146-00448.

27 H. Hu, Recent Advances of Bioresponsive Nano-Sized Contrast Agents for Ultra-High-Field Magnetic Resonance Imaging, *Front. Chem.*, 2020, **8**, 1–20, DOI: 10.3389/fchem.2020.00203.

28 G. Barisano, F. Sepehrband, S. Ma, K. Jann, R. Cabeen, D. J. Wang, A. W. Toga and M. Law, Clinical 7 t MRi: Are we there yet? A review about magnetic resonance imaging at ultra-high field, *Br. J. Radiol.*, 2019, **92**, 20180492, DOI: 10.1259/bjr.20180492.

29 P. Fries, J. N. Morelli, F. Lux, O. Tillement, G. Schneider and A. Buecker, The issues and tentative solutions for contrast-enhanced magnetic resonance imaging at ultra-high field strength, *Wiley Interdiscip. Rev.: Nanomed. Nanobiotechnol.*, 2014, **6**, 559–573, DOI: 10.1002/wnan.1291.

30 Y. Cai, Y. Wang, H. Xu, C. Cao, R. Zhu, X. Tang, T. Zhang and Y. Pan, Positive magnetic resonance angiography using ultrafine ferritin-based iron oxide nanoparticles, *Nanoscale*, 2019, **11**, 2644–2654, DOI: 10.1039/c8nr06812g.

31 P. Caravan, C. T. Farrar, L. Frullano and R. Uppal, Influence of Molecular Parameters and Increasing Magnetic Field Strength on Relaxivity of Gadolinium- and Manganese-Based T1 Contrast Agents, *Contrast Media Mol. Imaging*, 2009, **4**, 89, DOI: 10.1002/cmmi.267.

32 Z. Liang, Q. Wang, H. Liao, M. Zhao, J. Lee, C. Yang, F. Li and D. Ling, Artificially engineered antiferromagnetic nanoprobes for ultra-sensitive histopathological level magnetic resonance imaging, *Nat. Commun.*, 2021, **12**, 3840, DOI: 10.1038/s41467-021-24055-2.

33 B. Bartolomei, A. Bogo, F. Amato, G. Ragazzon and M. Prato, Nuclear Magnetic Resonance Reveals Molecular Species in Carbon Nanodot Samples Disclosing Flaws, *Angew. Chem., Int. Ed.*, 2022, **61**, e202200038, DOI: 10.1002/anie.202200038.

34 P. Sharmiladevi, K. Girigoswami, V. Haribabu and A. Girigoswami, Nano-enabled theranostics for cancer, *Mater. Adv.*, 2021, **2**, 2876–2891, DOI: 10.1039/d1ma00069a.

35 E. Sturabotti, V. Di Lisio, L. Cardo, A. Camilli, E. Moretón Alfonsín, D. Cangialosi, A. Iturrospe Ibarra, A. Arbe and M. Prato, Water Permeates and Plasticizes Amorphous Carbon Dots: Unraveling the Inner Accessibility of the Nanoparticles by Glass Transition Studies, *Adv. Mater.*, 2025, e10992, DOI: 10.1002/adma.202510992.

36 E. Terreno, D. D. Castelli, A. Viale and S. Aime, Challenges for Molecular Magnetic Resonance Imaging, *Chem. Rev.*, 2010, **110**, 3019–3042, DOI: 10.1021/cr100025t.

37 T. Zhu, L. Cao, X. Li, Y. Du, H. Yan, Z. Chang, W.-F. Dong and L. Li, Multifunctional iron-doped carbon dots: Integration of fluorescence and magnetic resonance imaging for enhanced photodynamic therapy, *Sens. Actuators, B*, 2025, **424**, 136812, DOI: 10.1016/j.snb.2024.136812.

38 R. Qin, Y. Feng, D. Ding, L. Chen, S. Li, H. Deng, S. Chen, Z. Han, W. Sun and H. Chen, Fe-Coordinated Carbon Nanozyme Dots as Peroxidase-Like Nanozymes and Magnetic Resonance Imaging Contrast Agents, *ACS Appl. Bio Mater.*, 2021, **4**, 5520–5528, DOI: 10.1021/acsabm.1c00336.

39 T. Luo, Y. Nie, J. Lu, Q. Bi, Z. Cai, X. Song, H. Ai and R. Jin, Iron doped carbon dots based nanohybrids as a tetramodal imaging agent for gene delivery promotion and photothermal-chemodynamic cancer synergistic theranostics, *Mater. Des.*, 2021, **208**, 109878, DOI: 10.1016/j.matdes.2021.109878.

40 J. Wang, X. Hu, H. Ding, X. Huang, M. Xu, Z. Li, D. Wang, X. Yan, Y. Lu, Y. Xu, Y. Chen, P. C. Morais, Y. Tian, R. Q. Zhang and H. Bi, Fluorine and Nitrogen Co-Doped Carbon Dot Complexation with Fe(III) as a T1 Contrast Agent for Magnetic Resonance Imaging, *ACS Appl. Mater. Interfaces*, 2019, **11**, 18203–18212, DOI: 10.1021/acsami.9b03644.

41 Q. Huang, Y. Liu, L. Zheng, L. Wu, Z. Zhou, J. Chen, W. Chen and H. Zhao, Biocompatible iron(II)-doped carbon dots as T 1-weighted magnetic resonance contrast agents and fluorescence imaging probes, *Microchim. Acta*, 2019, **186**, 186–492, DOI: 10.1007/s00604-019-3593-4.

42 H. Yang, L. Liu, Z. Shu, W. Zhang, C. Huang, Y. Zhu, S. Li, W. Wang, G. Li, Q. Zhang, Q. Liu and G. Jiang, Magnetic iron oxide nanoparticles: An emerging threat for the environment and human health, *J Environ. Sci.*, 2025, **152**, 188–202, DOI: 10.1016/j.jes.2024.04.045.

43 M. Botta, C. F. G. C. Geraldes and L. Tei, High spin Fe(III)-doped nanostructures as T1 MR imaging probes, *WIREs Nanomed. Nanobiotechnol.*, 2023, **15**, e1858, DOI: 10.1002/wnan.1858.

44 C. Wetzl, C. Renero-Lecuna, L. Cardo, L. M. Liz-Marzán and M. Prato, Temperature-Dependent Luminescence of Nd3+-Doped Carbon Nanodots for Nanothermometry, *ACS Appl. Mater. Interfaces*, 2024, **16**, 35484–35493, DOI: 10.1021/acsami.4c07605.

45 R. Uzal-Varela, F. Lucio-Martínez, A. Nucera, M. Botta, D. Esteban-Gómez, L. Valencia, A. Rodríguez-Rodríguez and C. Platas-Iglesias, A systematic investigation of the NMR relaxation properties of Fe(iii)-EDTA derivatives and their potential as MRI contrast agents, *Inorg. Chem. Front.*, 2023, **10**, 1633–1649, DOI: 10.1039/d2qi02665a.

46 J. Wan, W. Cai, X. Meng and E. Liu, Monodisperse water-soluble magnetite nanoparticles prepared by polyol process for high-performance magnetic resonance imaging, *Chem. Commun.*, 2007, 5004–5006, DOI: 10.1039/b712795b.

47 D. Maity, S. N. Kale, R. Kaul-Ghanekar, J. M. Xue and J. Ding, Studies of magnetite nanoparticles synthesized by thermal decomposition of iron(III) acetylacetonate in tri (ethylene glycol), *J. Magn. Magn. Mater.*, 2009, **321**, 3093–3098, DOI: 10.1016/j.jmmm.2009.05.020.

48 B. Bartolomei, A. Bogo, F. Amato, G. Ragazzon and M. Prato, Nuclear Magnetic Resonance Reveals Molecular Species in Carbon Nanodot Samples Disclosing Flaws, *Angew. Chem., Int. Ed.*, 2022, **61**, e202200038, DOI: 10.1002/ange.202200038.

49 N. Ullal, R. Mehta and D. Sunil, Separation and purification of fluorescent carbon dots - an unmet challenge, *Analyst*, 2024, **149**, 1680–1700, DOI: 10.1039/d3an02134c.

50 B. Bartolomei and M. Prato, The Importance of the Purification Step and the Characterization of the Products in the Synthesis of Carbon Nanodots, *Small*, 2023, **19**, 2206714, DOI: 10.1002/smll.202206714.

51 M. Hanauer, S. Pierrat, I. Zins, A. Lotz and C. Sönnichsen, Separation of nanoparticles by gel electrophoresis according to size and shape, *Nano Lett.*, 2007, **7**, 2881–2885, DOI: 10.1021/nl071615y.

52 L. Morbiato, L. Cardo, E. Sturabotti, P. Gobbo, G. Filippini and M. Prato, Structure Matters: Tailored Graphitization of Carbon Dots Enhances Photocatalytic Performance, *ACS Nano*, 2025, **19**, 4887–4900, DOI: 10.1021/acsnano.4c16538.

53 G. Ragazzon, A. Cadranel, E. V. Ushakova, Y. C. Wang, D. M. Guldi, A. L. Rogach, N. A. Kotov and M. Prato, Optical processes in carbon nanocolloids, *Chem*, 2021, **7**, 606–628, DOI: 10.1016/j.chempr.2020.11.012.

54 B. van Dam, H. Nie, B. Ju, E. Marino, J. M. J. Paulusse, P. Schall, M. Li and K. Dohnalová, Excitation-Dependent Photoluminescence from Single-Carbon Dots, *Small*, 2017, **13**, 1702098, DOI: 10.1002/smll.201702098.

55 F. Yan, Z. Sun, H. Zhang, X. Sun, Y. Jiang and Z. Bai, The fluorescence mechanism of carbon dots, and methods for tuning their emission color: a review, *Microchim. Acta*, 2019, **186**, 583, DOI: 10.1007/s00604-019-3688-y.

56 M. L. Liu, B. B. Chen, C. M. Li and C. Z. Huang, Carbon dots: synthesis, formation mechanism, fluorescence origin and sensing applications, *Green Chem.*, 2019, **21**, 449–471, DOI: 10.1039/C8GC02736F.

57 P. Ghods, O. B. Isgor, J. R. Brown, F. Bensebaa and D. Kingston, XPS depth profiling study on the passive oxide film of carbon steel in saturated calcium hydroxide solution and the effect of chloride on the film properties, *Appl. Surf. Sci.*, 2011, **257**, 4669–4677, DOI: 10.1016/j.apsusc.2010.12.120.

58 T. Yamashita and P. Hayes, Analysis of XPS spectra of Fe2+ and Fe3+ ions in oxide materials, *Appl. Surf. Sci.*, 2008, **254**, 2441–2449, DOI: 10.1016/j.apsusc.2007.09.063.

59 Y. J. Kim and C. R. Park, Analysis of Problematic Complexing Behavior of Ferric Chloride with N, N-Dimethylformamide Using Combined Techniques of FT-IR, XPS, and TGA/DTG, *Inorg. Chem.*, 2002, **41**, 6211–6216, DOI: 10.1021/ic011306p.

60 M. C. Biesinger, B. P. Payne, A. P. Grosvenor, L. W. M. Lau, A. R. Gerson and R. S. C. Smart, Resolving surface chemical states in XPS analysis of first row transition metals, oxides and hydroxides: Cr, Mn, Fe, Co and Ni, *Appl. Surf. Sci.*, 2011, **257**, 2717–2730, DOI: 10.1016/j.apsusc.2010.10.051.

61 W. Yang, T. T. Huang, M. Zhao, F. Luo, W. Weng, Q. Wei, Z. Lin and G. Chen, High peroxidase-like activity of iron and nitrogen co-doped carbon dots and its application in immunosorbent assay, *Talanta*, 2017, **164**, 1–6, DOI: 10.1016/j.talanta.2016.10.099.

62 X. Li, S. Ding, Z. Lyu, P. Tieu, M. Wang, Z. Feng, X. Pan, Y. Zhou, X. Niu, D. Du, W. Zhu and Y. Lin, Single-Atomic Iron Doped Carbon Dots with Both Photoluminescence and Oxidase-Like Activity, *Small*, 2022, **18**, 2203001, DOI: 10.1002/smll.202203001.

63 L. K. Plummer and J. E. Hutchison, Understanding the Effects of Iron Precursor Ligation and Oxidation State Leads to Improved Synthetic Control for Spinel Iron Oxide Nanocrystals, *Inorg. Chem.*, 2020, **59**, 15074–15087, DOI: 10.1021/acs.inorgchem.0c02040.

64 T. V. de Medeiros, J. Manioudakis, F. Noun, J.-R. Macairan, F. Victoria and R. Naccache, Microwave-Assisted Synthesis of Carbon Dots and Their Applications, *J. Mater. Chem. C*, 2019, **7**, 7175–7195, DOI: 10.1039/C9TC01640F.

65 Z. Zhao, M. Li, J. Zeng, L. Huo, K. Liu, R. Wei, K. Ni and J. Gao, Recent advances in engineering iron oxide nanoparticles for effective magnetic resonance imaging, *Bioact. Mater.*, 2022, **12**, 214–245, DOI: 10.1016/j.bioactmat.2021.10.014.

66 N. Ullal, R. Mehta and D. Sunil, Separation and purification of fluorescent carbon dots - an unmet challenge, *Analyst*, 2024, **149**, 1680–1700, DOI: 10.1039/d3an02134c.

67 Y. Hu, O. Seivert, Y. Tang, H. E. Karahan and A. Bianco, Carbon Dot Synthesis and Purification: Trends, Challenges and Recommendations, *Angew. Chem., Int. Ed.*, 2024, **63**, e202412341, DOI: 10.1002/anie.202412341.

68 M. Cho, J. Villanova, D. M. Ines, J. Chen, S. S. Lee, Z. Xiao, X. Guo, J. A. Dunn, D. D. Stueber, P. Decuzzi and V. L. Colvin, Sensitive T2 MRI Contrast Agents from the Rational Design of Iron Oxide Nanoparticle Surface Coatings, *J. Phys. Chem. C*, 2023, **127**, 1057–1070, DOI: 10.1021/acs.jpcc.2c05390.

69 Y. Lu, Y.-J. Xu, G. Zhang, D. Ling, M. Wang, Y. Zhou, Y.-D. Wu, T. Wu, M. J. Hackett, B. H. Kim, H. Chang, J. Kim, X.-T. Hu, L. Dong, N. Lee, F. Li, J.-C. He, L. Zhang, H.-Q. Wen, B. Yang, S. H. Choi, T. Hyeon and D.-H. Zou, Iron oxide nanoclusters for T1 magnetic resonance imaging of non-human primates, *Nat. Biomed. Eng.*, 2017, **1**, 637–643, DOI: 10.1038/s41551-017-0116-7.

70 L. Fernández-Méndez, Y. Fernández-Afonso, P. Martínez-Vicente, A. Urkola-Arsuaga, C. Miranda-Pérez de Alejo, I. L. de la Pisa, S. Plaza-García, J. Ruíz-Cabello, P. Ramos-Cabrer, L. Gutiérrez and S. Carregal-Romero, NIR-II Photoresponsive Magnetoliposomes for Remote-Controlled Release and Magnetic Resonance Imaging, *ACS Appl. Bio Mater.*, 2025, **8**, 4855–4869, DOI: 10.1021/acsabm.5c00233.

71 C. Chen, J. Ge, Y. Gao, L. Chen, J. Cui, J. Zeng and M. Gao, Ultrasmall superparamagnetic iron oxide nanoparticles: A next generation contrast agent for magnetic resonance imaging, *WIREs Nanomed. Nanobiotechnol.*, 2022, **14**, e1740, DOI: 10.1002/wnan.1740.

72 M. Rohrer, H. Bauer, J. Mintorovitch, M. Requardt and H.-J. Weinmann, Comparison of magnetic properties of MRI contrast media solutions at different magnetic field strengths, *Invest. Radiol.*, 2005, **40**, 715–724, DOI: 10.1097/01.rli.0000184756.66360.d3.

73 P. Szomolanyi, M. Rohrer, T. Frenzel, I. M. Noebauer-Huhmann, G. Jost, J. Endrikat, S. Trattnig and H. Pietsch, Comparison of the Relaxivities of Macrocyclic Gadolinium-Based Contrast Agents in Human Plasma at 1.5, 3, and 7 T, and Blood at 3 T, *Invest. Radiol.*, 2019, **54**, DOI: 10.1097/RLI.0000000000000577.

74 L. Helm, Optimization of Gadolinium-Based Mri Contrast Agents for High Magnetic-Field Applications, *Future Med. Chem.*, 2010, **2**, 385–396, DOI: 10.4155/fmc.09.174.

75 J. Wang, Y. Jia, Q. Wang, Z. Liang, G. Han, Z. Wang, J. Lee, M. Zhao, F. Li, R. Bai and D. Ling, An Ultrahigh-Field-Tailored T1–T2 Dual-Mode MRI Contrast Agent for High-Performance Vascular Imaging, *Adv. Mater.*, 2021, **33**, 2004917, DOI: 10.1002/adma.202004917.

76 T. Vangijzegem, D. Stanicki, S. Boutry, Q. Paternoster, L. Vander Elst, R. N. Muller and S. Laurent, VSION as high field MRI T1 contrast agent: Evidence of their potential as positive contrast agent for magnetic resonance angiography, *Nanotechnology*, 2018, **29**, 265103, DOI: 10.1088/1361-6528/aabbd0.

77 L. Faucher, M. Tremblay, J. Lagueux, Y. Gossuin and M. A. Fortin, Rapid synthesis of PEGylated ultrasmall gadolinium oxide nanoparticles for cell labeling and tracking with MRI, *ACS Appl. Mater. Interfaces*, 2012, **4**, 4506–4515, DOI: 10.1021/am3006466.

78 R. Marasini, S. Rayamajhi, A. Moreno-Sanchez and S. Aryal, Iron(III) chelated paramagnetic polymeric nanoparticle formulation as a next-generation: T 1-weighted MRI contrast agent, *RSC Adv.*, 2021, **11**, 32216–32226, DOI: 10.1039/d1ra05544e.

79 S. Laurent, L. Vander Elst and R. N. Muller, Comparative study of the physicochemical properties of six clinical low molecular weight gadolinium contrast agents, *Contrast Media Mol. Imaging*, 2006, **1**, 128–137, DOI: 10.1002/cmmi.100.

80 S. Noordin, C. S. Winalski, S. Shortkroff and R. V. Mulkern, Factors affecting paramagnetic contrast enhancement in synovial fluid: effects of electrolytes, protein concentrations, and temperature on water proton relaxivities from Mn ions and Gd chelated contrast agents, *Osteoarthritis Cartilage*, 2010, **18**, 964–970, DOI: 10.1016/j.joca.2010.03.010, DOI: 10.1016/j.addr.2025.115659.